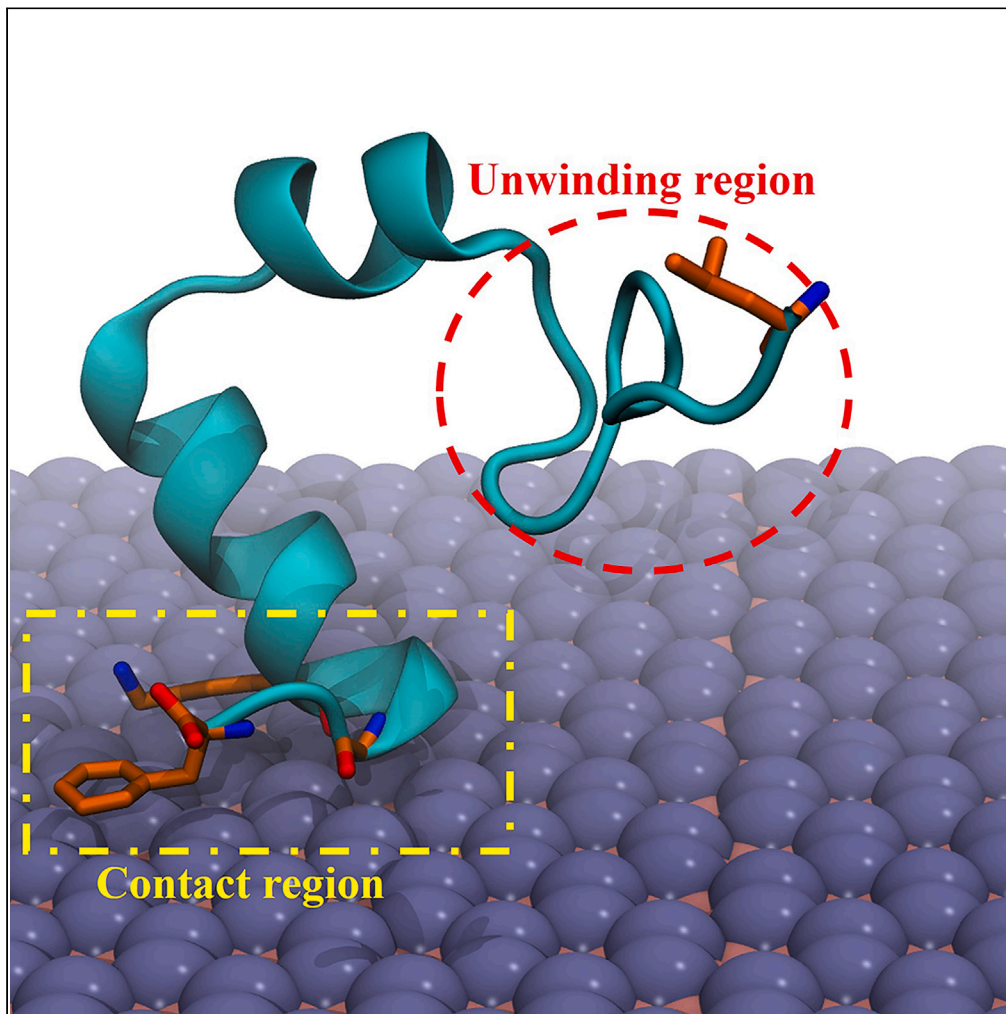**CellPress**
OPEN ACCESS

Article

Villin headpiece unfolding upon binding to boridene mediated by the ''anchoring-perturbation'' mechanism

Yuqi Luo, Zonglin Gu, Weihua Liao, Yiwen Huang, Jose Manuel Perez-Aguilar, Yanbo Luo, Longzhen Chen

luoyuqi2004@tom.com (Y.L.)
longzhenchen@126.com (L.C.)

Highlights
The interaction between boridene and HP35 is investigated using MD simulation approach

HP35 can unfold on boridene via "non-contact" mode

The "non-contact" mode denotes "anchoring-perturbation" mechanism

The potential toxicity of boridene to HP35 protein is revealed

iScience

Article

Villin headpiece unfolding upon binding
to boridene mediated
by the ''anchoring-perturbation'' mechanism

Yuqi Luo,[1,6,*] Zonglin Gu,[2] Weihua Liao,[3] Yiwen Huang,[4] Jose Manuel Perez-Aguilar,[5] Yanbo Luo,[1]
and Longzhen Chen[1,*]

SUMMARY

We employ molecular dynamics (MD) simulations to investigate the influence of boridene on the behavior of a protein model, HP35, with the aim of assessing the potential biotoxicity of boridene. Our MD results reveal that HP35 can undergo unfolding via an "anchoring-perturbation" mechanism upon adsorption onto the boridene surface. Specifically, the third helix of HP35 becomes tightly anchored to the boridene surface through strong electrostatic interactions between the abundant molybdenum atoms on the boridene surface and the oxygen atoms on the HP35 backbone. Meanwhile, the first helix, experiencing continuous perturbation from the surrounding water solution over an extended period, suffers from potential breakage of hydrogen bonds, ultimately resulting in its unfolding. Our findings not only propose, for the first time to our knowledge, the "anchoring-perturbation" mechanism as a guiding principle for protein unfolding but also reveal the potential toxicity of boridene on protein structures.

INTRODUCTION

With the rapid advancement of nanotechnology, nanomaterials have found extensive utilization across various scientific domains, including energy, electronics, optics, and medicine.[1–8] Among these, carbon-based nanomaterials (CBNs) have emerged as exceptional entities, possessing remarkable mechanical, optical, and electrical properties.[9–16] This has garnered significant attention, particularly in the field of biomedicine, encompassing gene delivery, optical imaging, and nanotherapeutics,[17–24] since the initial discovery of fullerene C60 in 1985,[25] carbon nanotubes (CNTs) in 1991,[26] and graphene in 2004.[27] With regard to biomedical applications, CBNs have exhibited great potential for integration into biological systems. However, the integration of foreign nanomaterials with living cells raises concerns regarding their potential impact on the integrity of the biomolecules, including cell membranes, proteins, and nucleic acids. In general terms, the presence of nanomaterials in the cellular milieu could either originate potential toxicity arising from the breakdown of natural cellular substances or coexist with cell components without significant effects on cellular function, i.e., biocompatibility. In both cases, the exogenous nanomaterials interact with various biological entities, underscoring the critical role of nanomaterial-biomolecule interactions. For instance, direct adhesion of proteins/DNA to CBNs can induce toxicity by denaturing their native structures (e.g., secondary and tertiary structures).[28,29] Similarly, CNTs can disrupt normal signal transmission by occupying the active sites of cellular receptors, thereby dysregulating native ligand-receptor interactions.[30] Moreover, graphene nanosheets possess the ability to penetrate cell membranes, extracting substantial amounts of phospholipids through strong dispersion interactions, which can lead to toxicity and potential antibacterial properties.[31] In addition, graphene[32] (and other 2D materials, including phosphorene[33]) can be inserted into the protein-protein interface, destroying native interfacial protein-protein communication. To enhance the biocompatibility needed in biomedical applications, CBNs are often employed by incorporating surface modifications (e.g., functionalization with polyethylene glycol or serum proteins).[34]

Beyond CBNs, transition metal dichalcogenides, particularly molybdenum disulfide (MoS₂),[35] have emerged as promising nanomaterials sharing similar physicochemical characteristics. MoS₂ has shown potential in various biomedical applications,[36–42] including antibacterial and antifungal agents, biosensors (due to unique direct band gaps), photothermal and chemotherapeutic agents (owing to high near-infrared absorbance and extensive specific surface area), and as a contrast agent for X-ray tomography imaging. Recent studies have investigated

[1]Department of Gastrointestinal and Hepatobiliary Surgery, Shenzhen Longhua District Central Hospital, No. 187, Guanlan Road, Longhua District, Shenzhen, Guangdong Province 518110, China
[2]College of Physical Science and Technology, Yangzhou University, Jiangsu 225009, China
[3]Department of Radiology, Guangzhou Nansha District Maternal and Child Health Hospital, No. 103, Haibang Road, Nansha District, Guangzhou, Guangdong Province 511457, China
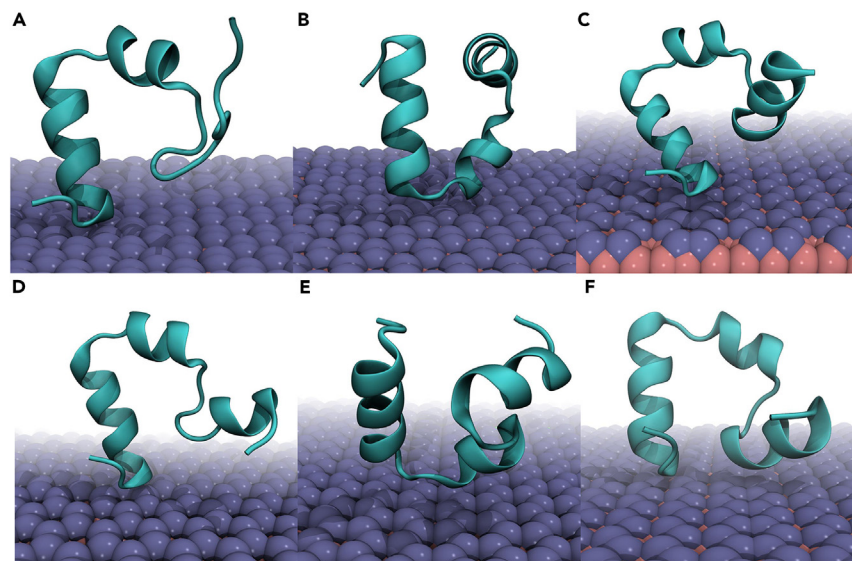[4]Department of Emergency, Nansha Hospital, Guangzhou First People's Hospital, Guangzhou, Guangdong, China
[5]School of Chemical Sciences, Meritorious Autonomous University of Puebla (BUAP), University City, Puebla 72570, Mexico
[6]Lead contact
*Correspondence: luoyuqi2004@tom.com (Y.L.), longzhenchen@126.com (L.C.)
https://doi.org/10.1016/j.isci.2023.108577

Figure 1. The final conformations of HP35 binding to boridene nanosheet at 2000 ns
(A–C) Three parallel simulations of sys-1.
(D–F) Three parallel simulations of sys-2. HP35 is shown with cyan cartoon representation, while boridene is presented with iceblue (Mo) and pink (B) spheres, respectively.

the direct interaction of MoS_2 with biomolecules,[43–45] revealing its capacity to alter protein structures due to strong attractive forces, suggesting its potential toxicity.

A member of the 2D nanomaterial family, called boridene,[46] has been successfully synthesized via chemical exfoliation, featuring ordered vacancies. Boridene, with a chemical formula of $Mo_{4/3}B_2$, comprises a layer of molybdenum atoms sandwiched between two layers of boron atoms (similar to a MoS_2 monolayer), with ordered and abundant vacancies present on both basal surfaces. In contrast to previous 2D nanomaterials such as graphene, graphene oxide, boron nitride, MoS_2, and MXene, boridene exhibits unique surface morphology characterized by ordered and abundant vacancies (grooves). Furthermore, the surface atoms of boridene consist of molybdenum atoms, carrying positive charges, a trait not observed in any previous 2D material. Despite some reported applications of boridene,[47–49] limited research has been conducted to investigate its potential nanotoxicology, a crucial aspect to consider. Additionally, the influence of the positively charged surface of boridene on the adsorption of globular proteins, although very intriguing, remains unknown. In this work, we reveal that the unique "anchoring-perturbation" mechanism mediates the unfolding of HP35, a prototypical globular protein, upon binding to boridene. As for this mechanism, the positively charged molybdenum atoms represent a significant role by robustly attracting the negatively charged oxygen atoms in the HP35 backbone.

RESULTS

The interaction of the globular protein HP35 with the boridene surface was investigated by unbiased molecular dynamics (MD) simulations. Three systems, namely sys-1, sys-2, and sys-3, were prepared with different orientations of the HP35 (see STAR Methods). For each system, three independent trajectories were carried out (see STAR Methods).

The final binding conformations of HP35 to the boridene surface from two independent simulations, sys-1 and sys-2, are depicted in Figure 1. Two distinct binding patterns are observed. In the first pattern, the third helical segment of HP35 comes into contact with the boridene surface, as illustrated in Figures 1A, 1C, 1E, and 1F. In the second pattern, the loop region that connects the second and third helices interacts with the boridene, as shown in Figures 1B and 1D. The results from the third simulation, sys-3, also present similar binding conformations (Figure S1). Regardless of the specific binding pattern, the interfacial interactions are remarkably stable (further details are in the following section). Interestingly, among the six final binding conformations, we observe the unfolding of HP35's first helix in the trajectory represented by Figure 1A, while the other structure of HP35 undergoes minimal changes upon binding to the boridene surface. It is intriguing that the unfolding event occurs at the first helix, which is not in direct contact with the boridene surface and experiences freedom of movement in the solution; the binding site is located at the third helix of HP35. Traditionally, the unfolding of HP35 takes place in the binding region, as demonstrated in previous studies involving graphene surface,[28] MoS_2 surface,[50] C_3N surface,[51] and boron nitride.[52] For example, the HP35 protein adsorbs on the graphene surface with the aromatic residue at the end of the third helix touching the graphene surface. Then, the third helix completely lies on the graphene surface, followed by the unfolding of this segment. However, no reports have yet revealed an unfolding event through a "non-contact" mode. In contrast, the additional simulation of an individual HP35 in solution (Figure S2)
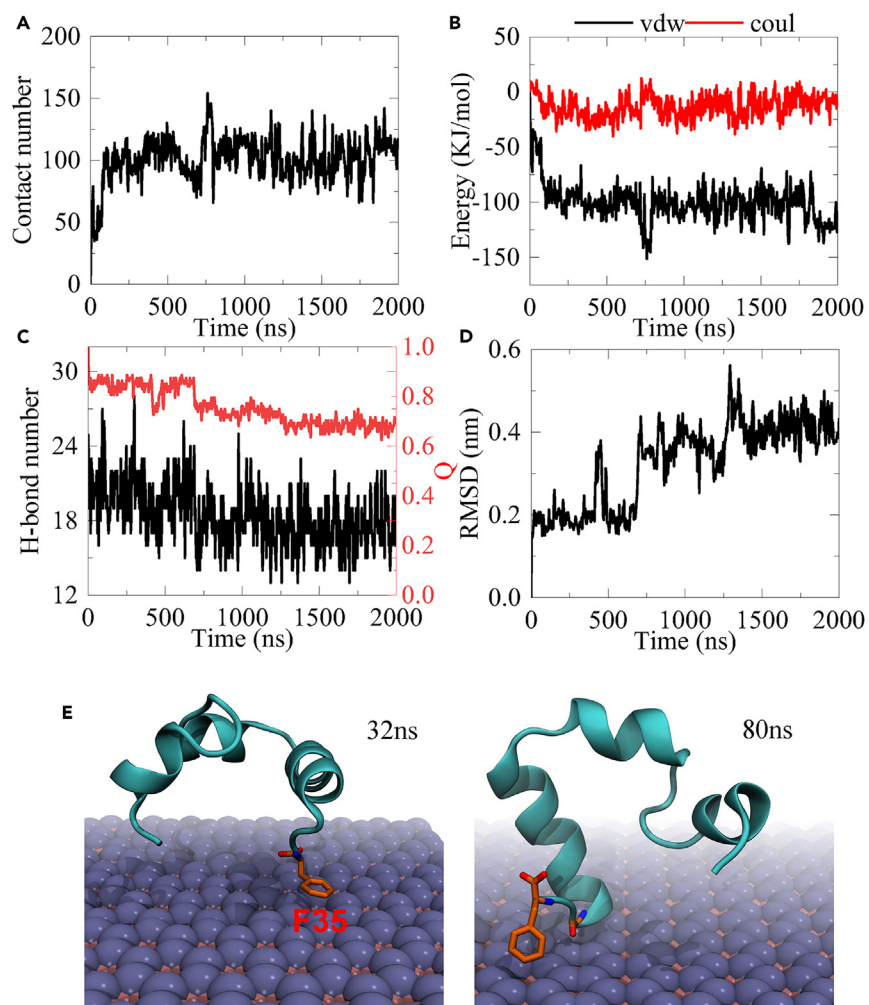
Figure 2. Binding kinetics of HP35 to boridene nanosheet in a typical trajectory

(A) Atom contact number of HP35 to boridene.

(B) Interaction energies, including van der Waals (vdW) and Coulomb (Coul) energies, between HP35 and boridene.

(C) Hydrogen bond (H-bond) number and Q value evolutions of HP35.

(D) Root-mean-square displacement (RMSD) of HP35.

(E) Two typical snapshots showing the binding process.

shows that HP35 almost maintains its entire structure throughout the 2000-ns simulation displaying low root-mean-square displacement (RMSD) values relative to the X-ray structure utilized.

Given that the first trajectory of sys-1 presents the most severe unfolding of HP35 among all trajectories, we select this representative trajectory (Figure 1A) for in-depth analysis (as shown in Figure 2) aiming at further elucidating the unfolding kinetics. Specifically, we calculate the interfacial atom contact number between HP35 and boridene, as well as the interaction energies (including van der Waals, vdW, and Coulomb energies) between the two entities. Additionally, we investigate the structural characteristics of HP35 during the adsorption process, such as the number of hydrogen bonds, the Q value, and the RMSD of HP35. The Q value represents the ratio of native contacts within residues as observed in the crystal structure. To calculate the Q value in the structures throughout the entire trajectory, a distance cutoff of 6 Å was used. We also include two snapshots at significant time points. Initially, at 32 ns, HP35 primarily attaches to the boridene surface via the F35 residue located at the end of the third helix. Notably, the aromatic phenyl ring of the F35 side chain exhibits a "face-to-face" interaction with the boridene surface positioning atop of it. At this stage, the interfacial interaction strengthens, resulting in an increased atom contact number to 41, accompanied by a sharp decrease in vdW energy to −36.2 kJ/mol while Coulomb energy has no distinct reduction. As time progresses to 80 ns, HP35 undergoes a rotation, leading to a relatively different orientation and binding pattern where the tail of HP35 (i.e., the end of the third helix) tightly adheres to the boridene surface. Subsequently, the binding site does not undergo any significant change. However, we observe a substantial structural change in HP35, specifically the unwinding of the first helical segment. Simultaneously, notable structural
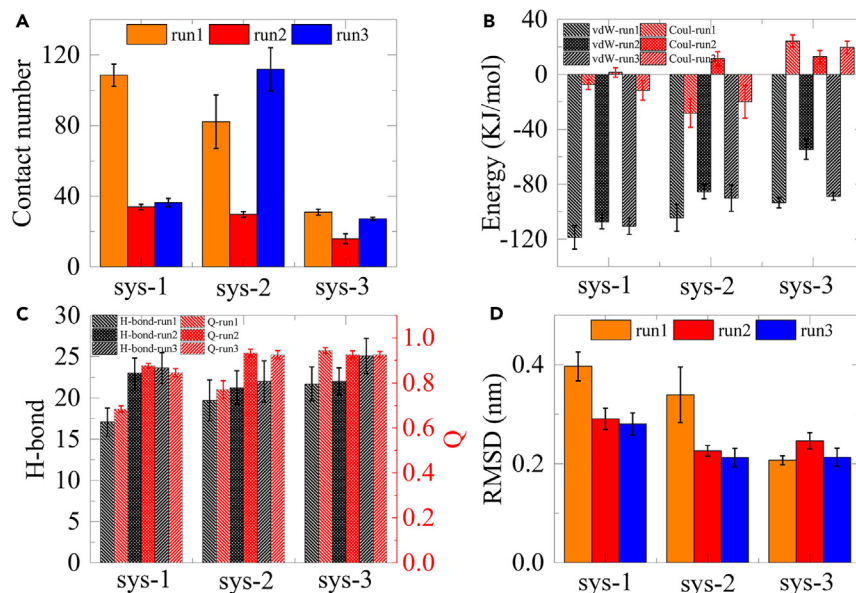
Figure 3. Statistical analysis of interaction between HP35 and boridene

(A) Mean contact number of HP35 binding to boridene.

(B) Mean interaction energies (including vdW and Coulomb energies) between HP35 and boridene.

(C) Mean hydrogen bond number of HP35.

(D) Mean RMSD of HP35. All data were calculated from the last 50 ns of each trajectory. The labels of run1, run2, and run3 indicate the first, second, and third trajectory of each system. Data are represented as mean ± SEM.

alterations in HP35 are observed, including a reduction in the number of hydrogen bonds from ∼23 to ∼18, a decline in the Q value to ∼0.8, and a final increase in RMSD values to ∼0.42 nm. These findings confirm the occurrence of severe structural denaturation in HP35 upon adsorption to the boridene surface, which supports the structural features depicted in Figure 1A. It is noteworthy that the interfacial interaction between HP35 and boridene stabilizes at 80 ns, while the unfolding of HP35 takes place after this time point. Furthermore, the unfolding predominantly affects the first helix (instead of the third helix), which is located distant from the interaction interface (also see Video S1), distinguishing it from previous studies.

Furthermore, to further confirm if the binding between HP35 and boridene was finally stable, we also calculated the RMSD of HP35 versus the boridene sheet as shown in Figures S3–S5. In most cases, the HP35 finally keeps stable after binding to boridene. We noted that Figure S3A shows a robust fluctuation. Although the interfacial binding of HP35 and boridene is completed, the fast movement of the first helix contributes to the continuous fluctuation of RMSD of HP35 versus boridene. The snapshots as shown in Figure S6 also clearly demonstrate the shift of the first helix.

We also conducted an analysis of other trajectories, as depicted in Figures S7–S14. The majority of these trajectories exhibit a weaker interaction between HP35 and boridene, characterized by lower atom contact numbers and interaction energies. However, we observe a contrasting behavior in the second and third trajectories of the sys-2 simulations. Specifically, in the second simulation of sys-1 (Figure S7) and the first simulation of sys-2 (Figure S9), the contact region was primarily located at the second helix of HP35 (refer to Figure 1). Notably, the contact number and interaction energies in this region are comparatively smaller. Similarly, in the third trajectory of sys-1 simulations (Figure S8), adsorption occurs exclusively at the third helix of HP35, resulting in limited interfacial contact. Conversely, in the second (Figure S10) and third (Figure S11) simulations of sys-2, HP35 interacts with boridene through its third and first helices, leading to slightly higher atom contact numbers and interaction energies, comparable to those observed for the other systems as shown in Figure 2. Three trajectories in the simulations of sys-3 also present weak interaction with boridene (Figures S12–S14). Furthermore, it is worth mentioning that among these trajectories, we observe a slight unwinding of the first helix of HP35 (refer to Figure 1; Figure S15) in the first trajectory of the sys-2 simulation. Additionally, the analysis of hydrogen bonds and Q evolutions (Figure S9) in this particular trajectory indicates a slight reduction compared to the other trajectories. Moreover, higher RMSD values were also detected. The binding dynamics (and unfolding process) are illustrated in Figure S16, wherein the unfolding region is located at the first helix while the binding region is in the third helix, also confirming the "anchoring-perturbation" mechanism. In addition, we also performed an additional simulation of the sys-1 systems and found again the local unfolding event. As shown in Figure S17, the hydrogen bond number and Q value of HP35 decline after 400 ns, while the RMSD values increase. HP35 shows denaturation at the first helix while the loop segment that connects the second and third helices remains anchored on the boridene surface. These results also support and strengthen the "anchoring-perturbation" mechanism guiding HP35 unfolding as discovered previously. We also summarized the interaction features between HP35 and the boridene surface as well as the structural changes
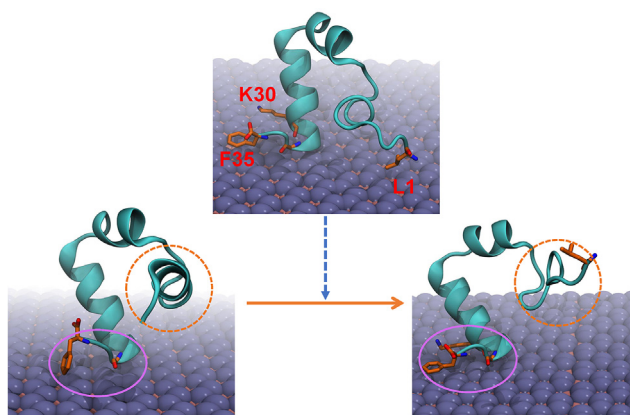
**Figure 4. HP35 unfolding mechanism on boridene surface**

Left: Initial configuration of HP35 on boridene before protein unfolding. Right: Final configuration of HP35 on boridene after protein unfolding. Upper: Middle configuration of HP35 on boridene with some typical residues highlighted. The purple curve indicates the anchoring region of HP35 on boridene, and the orange dashed curve denotes the free movement region of HP35 in the solution.

of HP35 by calculating the corresponding data at the last 50 ns of each trajectory as shown in Figure 3. From the contact number results, the first trajectory of sys-1 and the first and third trajectories of sys-2 show significant values due to the strong interfacial contact. The interaction energy profiles denote that the vdW interaction mainly determines the binding of the HP35 protein on boridene. Hydrogen bond and Q value analysis of HP35 demonstrate that the first trajectories of sys-1 and sys-2 both present lower values compared to other trajectories, confirming the denaturation process of HP35 in these two simulations as mentioned previously. Similarly, the RMSD of HP35 in the first trajectories of sys-1 and sys-2 exhibit higher values in comparison with other trajectories, further supporting the local unwinding of HP35 in these two trajectories. These findings suggest that the denaturation of HP35 upon stable direct contact with the boridene surface exhibits a certain degree of contingency. However, it is important to note that at least local helical content loss can possibly occur.

To elucidate the underlying mechanism behind the unfolding event on the first helix of HP35, induced by non-direct contact, critical snapshots are presented in Figure 4. Interestingly, upon comparing the conformations of HP35 before and after unfolding, we consistently observe the interaction region positioned at the end of the third helix, with limited perturbation in orientation. In contrast, the first helix of HP35 undergoes substantial unraveling, resulting in the loss of its original secondary structure helical content into a curved conformation. Therefore, the likely reason driving the non-direct-contact-induced unfolding is the tight anchoring of the end of the third helix on the boridene surface, while the first helix freely moves in the solution and is perturbed by it. During this process, where the third helix remains fixed and the first helix experiences perturbation from the solution, the first helix undergoes persistent perturbation while the third helix is effectively immobilized on the boridene surface. Consequently, the first helix unwinds. Moreover, during this process, direct contact between residue L1 (in the first helix) and the boridene surface further intensifies the unfolding of the first helix, exerting a stretching force that contributes to the unwinding.

To examine how the third helix becomes fixed on the boridene surface, we conducted additional analyses and calculations. Firstly, we calculated the contact probability of each residue of HP35 with the boridene surface, as depicted in Figure 5A. Clearly, residues spanning from 29 to 35 exhibit relatively high contact probabilities, indicating a preferential binding capacity of the third helix to the boridene surface. We also observed that residue L1 possesses a non-negligible contact probability, confirming the finding depicted in Figure 4, where this residue occasionally contacts the boridene surface. Subsequently, the residues in the third helix with high contact probabilities were traced by projecting the center of mass of this region onto the x-y plane (i.e., the boridene surface) from 0 to 2000 ns (as shown in Figure 5B). Evidently, this segment exhibits a relatively concentrated distribution, suggesting that the third helix of HP35 is almost immobile on the boridene surface with limited lateral displacement. One might question why the third helix can be effectively immobilized on the boridene surface. To shed light on this matter, we zoomed in on the HP35-boridene interface to examine the local binding conformation of the HP35 backbone (Figure 5C). Interestingly, we discovered that the oxygen atoms in the HP35 backbone form close and tight connections with the boridene surface's Mo atoms. Further calculations demonstrated strong electrostatic interactions (Coulomb energy) between these oxygen atoms and the surface Mo atoms, owing to the negative charges of oxygen and positive charges of Mo. In particular, this electrostatic force reaches approximately −50 kJ/mol, resulting from the abundance of Mo on the boridene surface. In other words, the negatively charged oxygen atom on the third helix of HP35 can be robustly captured by and simultaneously anchored to the boridene surface through the strong electrostatic interaction, as the third helix remains fully anchored. As a consequence, the first helix, subjected to continuous perturbation from the water solution over an extended period, experiences potential breakage of hydrogen bonds, eventually leading to its unfolding. In contrast, HP35 can freely move on graphene,[28] C_3N,[51] and boron nitride[52] surfaces.

Finally, we present the structures of HP35 at ten different time points, selected from 100 to 1900 ns with intervals of 200 ns. Subsequently, we align all HP35 structures by superimposing the third helices (the anchoring region) together, as shown in Figure 6. Consistent with our previous findings, the third helices in the ten structures can be almost seamlessly merged, indicating that the third helix, which directly
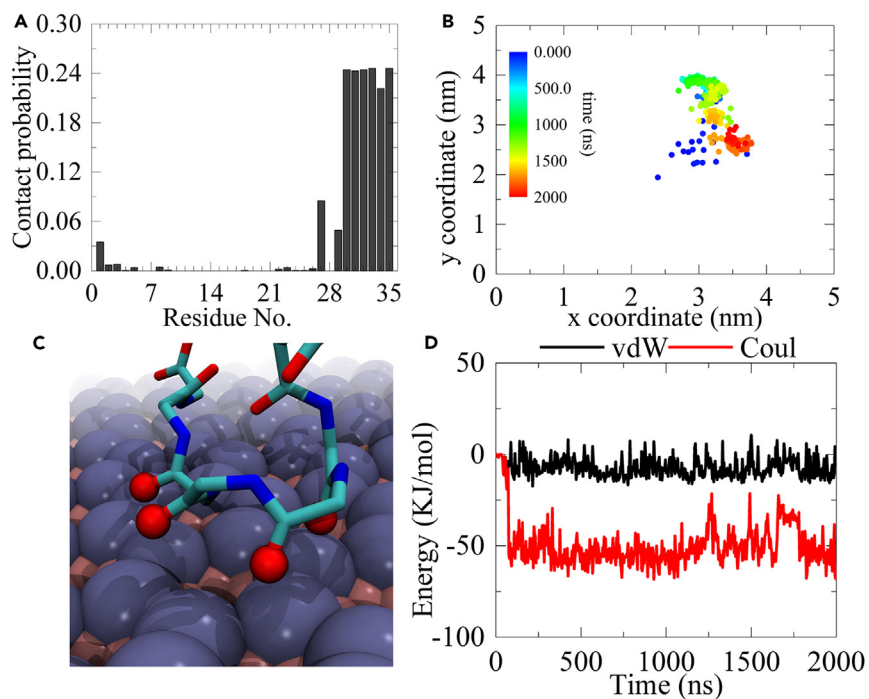
Figure 5. Detailed analysis of the anchoring region of HP35 on boridene in the typical trajectory

(A) Contact probability of each residue of HP35 binding to boridene.

(B) Time-dependent coordinate evolutions of the anchoring region of HP35 projecting onto boridene surface (i.e., x-y plane).

(C) Typical snapshot showing the local binding configuration of oxygen atom on the protein backbone to boridene surface. The critical oxygen atoms on the protein backbone are shown with red spheres while the entire backbone is illustrated with sticks.

(D) Time-dependent interaction energies between four selected oxygen atoms in (C) and boridene.

interacts with the boridene surface, exhibits minimal structural changes. Similarly, the second helix remains largely unchanged. However, the third helix gradually diminishes as the simulation progresses, eventually adopting an irregular structure. Furthermore, the first helix freely moves in the solution without a fixed orientation. This analysis further supports the "anchoring-perturbation" mechanism underlying the unfolding of HP35.

DISCUSSION

In summary, we utilize MD simulations to explore the potential toxicity of boridene by investigating the interaction between the HP35 globular protein and a boridene nanosheet. Our simulations demonstrate that the binding of HP35 to the boridene surface leads to a loss in the secondary structural content, particularly, the unwinding of helical structure. Notably, the unfolding primarily occurs in the first helix, even though direct contact with the nanostructure occurs in the third helix. Further analysis reveals that the strong electrostatic interaction between the negatively charged oxygen atoms in the backbone of the third helix of HP35 and the molybdenum atoms on the boridene structure allows for the robust anchoring of the third helix on the surface. Consequently, the first helix, subjected to continuous perturbation from the surrounding water solution over an extended period, undergoes potential breakage of hydrogen bonds, ultimately resulting in its unfolding.
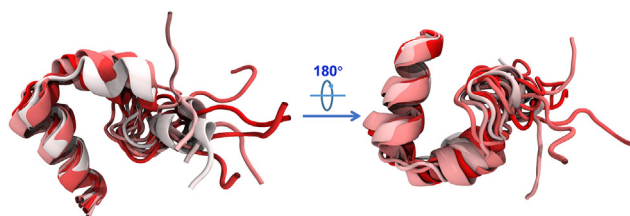
Figure 6. Alignment of HP35 structures at 10 time points (from 100 to 1900 with an interval of 200 ns) via aligning the anchoring region of HP35 together

The HP35 colors from white to red indicate the time from 100 to 1900 ns.

This unfolding mechanism, characterized as the "anchoring-perturbation" mechanism, highlights an observation whereby the unfolding of HP35 occurs at a distance from the direct contact-binding site. Our findings provide insights into the understanding of protein unfolding when interacting with nanomaterials, emphasizing the importance of considering such mechanisms in the study of nanotoxicology.

Considering the potential toxicity of boridene to the HP35 protein, certain pretreatments should be administered before utilizing this material in various bioapplications, such as nanocarriers. Drawing inspiration from graphene-based materials, we propose a strategy involving the pretreatment of surface coatings or functionalizations on boridene (e.g., PEG, chitosan, and protein corona) prior to its use in experiments.[53–55]

Limitations of the study

Our MD results provide insights into the potential toxicity of boridene to protein. The determination of such toxicity can be further verified by experiments, for instance, the loss of the helical secondary structure content of HP35 in the presence of the nanomaterial.

STAR★METHODS

Detailed methods are provided in the online version of this paper and include the following:

- KEY RESOURCES TABLE
- RESOURCE AVAILABILITY
  - Lead contact
  - Materials availability
  - Data and code availability
- METHOD DETAILS
  - Simulation setup
  - Simulation protocol

SUPPLEMENTAL INFORMATION

Supplemental information can be found online at https://doi.org/10.1016/j.isci.2023.108577.

AUTHOR CONTRIBUTIONS

Y.L. and L.C. conceived the concept and designed the study. Y.L. and Z.G. carried out the theoretical calculations and analysis. Y.L., Z.G., J.M.P.-A., W.L., Y.H., Y.L., and L.C. co-wrote the paper. All authors discussed the results and commented on the manuscript.

DECLARATION OF INTERESTS

The authors declare no competing financial interest.

REFERENCES

1. Das, A., Pisana, S., Chakraborty, B., Piscanec, S., Saha, S.K., Waghmare, U.V., Novoselov, K.S., Krishnamurthy, H.R., Geim, A.K., Ferrari, A.C., and Sood, A.K. (2008). Monitoring dopants by Raman scattering in an electrochemically top-gated graphene transistor. Nat. Nanotechnol. 3, 210–215.

2. Bolotin, K.I., Sikes, K.J., Jiang, Z., Klima, M., Fudenberg, G., Hone, J., Kim, P., and Stormer, H.L. (2008). Ultrahigh electron mobility in suspended graphene. Solid State Commun. 146, 351–355.

3. Liu, M., Yin, X., and Zhang, X. (2012). Double-Layer Graphene Optical Modulator. Nano Lett. 12, 1482–1485.

4. Jaramillo, T.F., Jorgensen, K.P., Bonde, J., Nielsen, J.H., Horch, S., and Chorkendorff, I. (2007). Identification of active edge sites for electrochemical H-2 evolution from MoS2 nanocatalysts. Science 317, 100–102.

5. Radisavljevic, B., Radenovic, A., Brivio, J., Giacometti, V., and Kis, A. (2011). Single-layer MoS2 transistors. Nat. Nanotechnol. 6, 147–150.

6. Wang, Q.H., Kalantar-Zadeh, K., Kis, A., Coleman, J.N., and Strano, M.S. (2012). Electronics and optoelectronics of

two-dimensional transition metal dichalcogenides. Nat. Nanotechnol. *7*, 699–712.

7. Jariwala, D., Sangwan, V.K., Lauhon, L.J., Marks, T.J., and Hersam, M.C. (2014). Emerging Device Applications for Semiconducting Two-Dimensional Transition Metal Dichalcogenides. ACS Nano *8*, 1102–1120.

8. Ghosh, A., Mukhopadhyay, T.K., and Datta, A. (2022). Two dimensional materials are non-nanotoxic and biocompatible towards cyclotides: evidence from classical molecular dynamics simulations. Nanoscale *15*, 321–336.

9. Sanchez, V.C., Jachak, A., Hurt, R.H., and Kane, A.B. (2012). Biological Interactions of Graphene-Family Nanomaterials: An Interdisciplinary Review. Chem. Res. Toxicol. *25*, 15–34.

10. Wang, J. (2005). Carbon-nanotube based electrochemical biosensors: A review. Electroanalysis *17*, 7–14.

11. Feng, L., and Liu, Z. (2011). Graphene in biomedicine: opportunities and challenges. Nanomedicine *6*, 317–324.

12. Katsnelson, M.I. (2007). Graphene: carbon in two dimensions. Mater. Today *10*, 20–27.

13. Geim, A.K. (2009). Graphene: Status and Prospects. Science *324*, 1530–1534.

14. Wang, C., Zhang, L., Guo, Z., Xu, J., Wang, H., Zhai, K., and Zhuo, X. (2010). A novel hydrazine electrochemical sensor based on the high specific surface area graphene. Microchim. Acta *169*, 1–6.

15. Coleman, J.N., Khan, U., Blau, W.J., and Gun'ko, Y.K. (2006). Small but strong: A review of the mechanical properties of carbon nanotube-polymer composites. Carbon *44*, 1624–1652.

16. Mukhopadhyay, T.K., Bhattacharyya, K., and Datta, A. (2018). Gauging the Nanotoxicity of h2D-C2N toward Single-Stranded DNA: An in Silico Molecular Simulation Approach. ACS Appl. Mater. Interfaces *10*, 13805–13818.

17. Cha, C., Shin, S.R., Annabi, N., Dokmeci, M.R., and Khademhosseini, A. (2013). Carbon-Based Nanomaterials: Multifunctional Materials for Biomedical Engineering. ACS Nano *7*, 2891–2897.

18. Bao, H., Pan, Y., Ping, Y., Sahoo, N.G., Wu, T., Li, L., Li, J., and Gan, L.H. (2011). Chitosan-Functionalized Graphene Oxide as a Nanocarrier for Drug and Gene Delivery. Small *7*, 1569–1578.

19. Li, B., Cheng, Y., Liu, J., Yi, C., Brown, A.S., Yuan, H., Tuan, V.-D., Fischer, M.C., and Warren, W.S. (2012). Direct Optical Imaging of Graphene In Vitro by Nonlinear Femtosecond Laser Spectral Reshaping. Nano Lett. *12*, 5936–5940.

20. Shao, Y., Wang, J., Wu, H., Liu, J., Aksay, I.A., and Lin, Y. (2010). Graphene Based Electrochemical Sensors and Biosensors: A Review. Electroanal *22*, 1027–1036.

21. Lee, J.S., Joung, H.-A., Kim, M.-G., and Park, C.B. (2012). Graphene-Based Chemiluminescence Resonance Energy Transfer for Homogeneous Immunoassay. ACS Nano *6*, 2978–2983.

22. Yang, K., Wan, J., Zhang, S., Tian, B., Zhang, Y., and Liu, Z. (2012). The influence of surface chemistry and size of nanoscale graphene oxide on photothermal therapy of cancer using ultra-low laser power. Biomaterials *33*, 2206–2214.

23. Yang, Z., Kang, S.-G., and Zhou, R. (2014). Nanomedicine: de novo design of nanodrugs. Nanoscale *6*, 663–677.

24. Li, M., Yang, X., Ren, J., Qu, K., and Qu, X. (2012). Using Graphene Oxide High Near-Infrared Absorbance for Photothermal Treatment of Alzheimer's Disease. Adv. Mater. *24*, 1722–1728.

25. Kroto, H.W., Heath, J.R., Obrien, S.C., Curl, R.F., and Smalley, R.E. (1985). C_{60}: Buckminsterfullerene. Nature *318*, 162–163.

26. Iijima, S. (1991). Helical Microtubes of Graphitic Carbon. Nature *354*, 56–58.

27. Novoselov, K.S., Geim, A.K., Morozov, S., Jiang, D., Zhang, Y., Dubonos, S.a., Grigorieva, I., and Firsov, A. (2004). Electric field effect in atomically thin carbon films. Science *306*, 666–669.

28. Zuo, G., Zhou, X., Huang, Q., Fang, H.P., and Zhou, R.H. (2011). Adsorption of Villin Headpiece onto Graphene, Carbon Nanotube, and C60: Effect of Contacting Surface Curvatures on Binding Affinity. J. Phys. Chem. C *115*, 23323–23328.

29. Kong, Z., Hu, W., Jiao, F.F., Zhang, P.Z., Shen, J.W., Cui, B., Wang, H.B., and Liang, L.J. (2020). Theoretical Evaluation of DNA Genotoxicity of Graphene Quantum Dots: A Combination of Density Functional Theory and Molecular Dynamics Simulations. J. Phys. Chem. B *124*, 9335–9342.

30. Zuo, G.H., Gu, W., Fang, H.P., and Zhou, R.H. (2011). Carbon Nanotube Wins the Competitive Binding over Proline-Rich Motif Ligand on SH3 Domain. J. Phys. Chem. C *115*, 12322–12328.

31. Tu, Y.S., Lv, M., Xiu, P., Huynh, T., Zhang, M., Castelli, M., Liu, Z.R., Huang, Q., Fan, C.H., Fang, H.P., and Zhou, R.H. (2013). Destructive extraction of phospholipids from Escherichia coli membranes by graphene nanosheets. Nat. Nanotechnol. *8*, 594–601.

32. Luan, B.Q., Huynh, T., Zhao, L., and Zhou, R.H. (2015). Potential Toxicity of Graphene to Cell Functions via Disrupting Protein-Protein Interactions. ACS Nano *9*, 663–669.

33. Mukhopadhyay, T.K., Ghosh, A., and Datta, A. (2021). Molecular Dynamics Simulations Reveal Orientation-Dependent Nanotoxicity of Black Phosphorene toward Dimeric Proteins. ACS Appl. Nano Mater. *4*, 3095–3107.

34. Ge, C., Du, J., Zhao, L., Wang, L., Liu, Y., Li, D., Yang, Y., Zhou, R., Zhao, Y., Chai, Z., and Chen, C. (2011). Binding of blood proteins to carbon nanotubes reduces cytotoxicity. Proc. Natl. Acad. Sci. USA *108*, 16968–16973.

35. Coleman, J.N., Lotya, M., O'Neill, A., Bergin, S.D., King, P.J., Khan, U., Young, K., Gaucher, A., De, S., Smith, R.J., et al. (2011). Two-Dimensional Nanosheets Produced by Liquid Exfoliation of Layered Materials. Science *331*, 568–571.

36. Yang, X., Li, J., Liang, T., Ma, C., Zhang, Y., Chen, H., Hanagata, N., Su, H., and Xu, M. (2014). Antibacterial activity of two-dimensional MoS2 sheets. Nanoscale *6*, 10126–10133.

37. Wang, S., Li, K., Chen, Y., Chen, H., Ma, M., Feng, J., Zhao, Q., and Shi, J. (2015). Biocompatible PEGylated MoS2 nanosheets: Controllable bottom-up synthesis and highly efficient photothermal regression of tumor. Biomaterials *39*, 206–217.

38. Liu, T., Wang, C., Cui, W., Gong, H., Liang, C., Shi, X., Li, Z., Sun, B., and Liu, Z. (2014). Combined photothermal and photodynamic therapy delivered by PEGylated MoS2 nanosheets. Nanoscale *6*, 11219–11225.

39. Wang, L., Wang, Y., Wong, J.I., Palacios, T., Kong, J., and Yang, H.Y. (2014). Functionalized MoS2 Nanosheet-Based Field-Effect Biosensor for Label-Free Sensitive Detection of Cancer Marker Proteins in Solution. Small *10*, 1101–1105.

40. Yin, W., Yan, L., Yu, J., Tian, G., Zhou, L., Zheng, X., Zhang, X., Yong, Y., Li, J., Gu, Z., and Zhao, Y. (2014). High-Throughput Synthesis of Single-Layer MoS2 Nanosheets as a Near-Infrared Photothermal-Triggered Drug Delivery for Effective Cancer Therapy. ACS Nano *8*, 6922–6933.

41. Liu, T., Shi, S., Liang, C., Shen, S., Cheng, L., Wang, C., Song, X., Goel, S., Barnhart, T.E., Cai, W., and Liu, Z. (2015). Iron Oxide Decorated MoS2 Nanosheets with Double PEGylation for Chelator-Free Radio labeling and Multimodal Imaging Guided Photothermal Therapy. ACS Nano *9*, 950–960.

42. Zhu, C., Zeng, Z., Li, H., Li, F., Fan, C., and Zhang, H. (2013). Single-Layer MoS2-Based Nanoprobes for Homogeneous Detection of Biomolecules. J. Am. Chem. Soc. *135*, 5998–6001.

43. Gu, Z., Li, W., Hong, L., and Zhou, R. (2016). Exploring biological effects of MoS2 nanosheets on native structures of α-helical peptides. J. Chem. Phys. *144*, 175103.

44. Ling, Y., Gu, Z., Kang, S.-G., Luo, J., and Zhou, R. (2016). Structural Damage of a beta-Sheet Protein upon Adsorption onto Molybdenum Disulfide Nanotubes. J. Phys. Chem. C *120*, 6796–6803.

45. Gu, Z., De Luna, P., Yang, Z., and Zhou, R. (2017). Structural influence of proteins upon adsorption to MoS2 nanomaterials: comparison of MoS2 force field parameters. Phys. Chem. Chem. Phys. *19*, 3039–3045.

46. Zhou, J., Palisaitis, J., Halim, J., Dahlqvist, M., Tao, Q., Persson, I., Hultman, L., Persson, P.O., and Rosen, J. (2021). Boridene: Two-dimensional Mo4/3B2-x with ordered metal vacancies obtained by chemical exfoliation. Science *373*, 801–805.

47. Helmer, P., Halim, J., Zhou, J., Mohan, R., Wickman, B., Björk, J., and Rosen, J. (2022). Investigation of 2D Boridene from First Principles and Experiments. Adv. Funct. Mater. *32*, 2109060.

48. He, S., and Gu, Z. (2023). Efficient seawater desalination in lamellar nanochannel-based boridene filtration membrane. Phys. Chem. Chem. Phys. *25*, 11261–11267.

49. Chen, B., Liu, H., Bai, T., Song, Z., Xie, J., Wu, K., Cheng, Y., and Xiao, B. (2022). Prediction of boridenes as high-performance anodes for alkaline metal and alkaline Earth metal ion batteries. Nanoscale *14*, 17955–17975.

50. Gu, Z., Yang, Z., Kang, S.-G., Yang, J.R., Luo, J., and Zhou, R. (2016). Robust Denaturation of Villin Headpiece by MoS2 Nanosheet: Potential Molecular Origin of the Nanotoxicity. Sci. Rep. *6*, 28252.

51. Gu, Z.L., Perez-Aguilar, J.M., Meng, L.J., and Zhou, R.H. (2020). Partial Denaturation of Villin Headpiece upon Binding to a Carbon Nitride Polyaniline (C3N) Nanosheet. J. Phys. Chem. B *124*, 7557–7563.

52. Luo, M., Yu, Y., Jin, Z., Dong, H.L., and Li, Y.Y. (2020). Multi-scale simulations on biocompatibility of boron nitride nanomaterials with different curvatures: A comparative study. Appl. Surf. Sci. *517*, 146181.

53. Wen, H.Y., Dong, C.Y., Dong, H.Q., Shen, A.J., Xia, W.J., Cai, X.J., Song, Y.Y., Li, X.Q., Li, Y.Y., and Shi, D.L. (2012). Engineered Redox-Responsive PEG Detachment Mechanism in PEGylated Nano-Graphene Oxide for Intracellular Drug Delivery. Small *8*, 760–769.

54. Yang, X.M., Tu, Y.F., Li, L.A., Shang, S.M., and Tao, X.M. (2010). Well-Dispersed Chitosan/Graphene Oxide Nanocomposites. ACS Appl. Mater. Interfaces *2*, 1707–1713.

55. Hu, W.B., Peng, C., Lv, M., Li, X.M., Zhang, Y.J., Chen, N., Fan, C.H., and Huang, Q. (2011). Protein Corona-Mediated Mitigation of Cytotoxicity of Graphene Oxide. ACS Nano *5*, 3693–3700.

56. Abraham, M.J., Murtola, T., Schulz, R., Páll, S., Smith, J.C., Hess, B., and Lindahl, E. (2015). GROMACS: High performance molecular simulations through multi-level parallelism from laptops to supercomputers. SoftwareX *1*, 19–25.

57. Humphrey, W., Dalke, A., and Schulten, K. (1996). VMD: Visual molecular dynamics. J. Mol. Graph. Model. *14*, 33–38.

58. Snow, C.D., Nguyen, N., Pande, V.S., and Gruebele, M. (2002). Absolute comparison of simulated and experimental protein-folding dynamics. Nature *420*, 102–106.

59. Shaw, D.E., Maragakis, P., Lindorff-Larsen, K., Piana, S., Dror, R.O., Eastwood, M.P., Bank, J.A., Jumper, J.M., Salmon, J.K., Shan, Y., and Wriggers, W. (2010). Atomic-Level Characterization of the Structural Dynamics of Proteins. Science *330*, 341–346.

60. Lei, H., Wu, C., Liu, H., and Duan, Y. (2007). Folding free-energy landscape of villin headpiece subdomain from molecular dynamics simulations. P. Natl. Acad. Sci. USA *104*, 4925–4930.

61. Chiu, T.K., Kubelka, J., Herbst-Irmer, R., Eaton, W.A., Hofrichter, J., and Davies, D.R. (2005). High-resolution x-ray crystal structures of the villin headpiece subdomain, an ultrafast folding protein. P. Natl Acad. Sci. USA *102*, 7517–7522.

62. Klauda, J.B., Venable, R.M., Freites, J.A., O'Connor, J.W., Tobias, D.J., Mondragon-Ramirez, C., Vorobyov, I., MacKerell, A.D., Jr., and Pastor, R.W. (2010). Update of the CHARMM All-Atom Additive Force Field for Lipids: Validation on Six Lipid Types. J. Phys. Chem. B *114*, 7830–7843.

63. Jorgensen, W.L., Chandrasekhar, J., Madura, J.D., Impey, R.W., and Klein, M.L. (1983). Comparison of Simple Potential Functions for Simulating Liquid Water. J. Chem. Phys. *79*, 926–935.

64. He, S.X., and Gu, Z.L. (2023). Efficient seawater desalination in lamellar nanochannel-based boridene filtration membrane. Phys. Chem. Chem. Phys. *25*, 11261–11267.

65. Van Gunsteren, W.F., and Berendsen, H.J. (1988). A leap-frog algorithm for stochastic dynamics. Mol. Sim. *1*, 173–185.

66. Bussi, G., Donadio, D., and Parrinello, M. (2007). Canonical sampling through velocity rescaling. J. Chem. Phys. *126*, 014101.

67. Parrinello, M., and Rahman, A. (1981). Polymorphic Transitions in Single-Crystals - A New Molecular-Dynamics Method. J. Appl. Phys. *52*, 7182–7190.

68. Darden, T., York, D., and Pedersen, L. (1993). Particle Mesh Ewald - An N.Log(N) Method for Ewald Sums in Large Systems. J. Chem. Phys. *98*, 10089–10092.

69. Essmann, U., Perera, L., Berkowitz, M.L., Darden, T., Lee, H., and Pedersen, L.G. (1995). A Smooth Particle Mesh Ewald Method. J. Chem. Phys. *103*, 8577–8593.

70. Hess, B., Bekker, H., Berendsen, H.J.C., and Fraaije, J. (1997). LINCS: A linear constraint solver for molecular simulations. J. Comput. Chem. *18*, 1463–1472.

71. Miyamoto, S., and Kollman, P.A. (1992). Settle - An Analytical Version of The Shake and Rattle Algorithm for Rigid Water Models. J. Comput. Chem. *13*, 952–962.

STAR★METHODS

KEY RESOURCES TABLE

REAGENT or RESOURCE	SOURCE	IDENTIFIER
Software and algorithms		
GROMACS version 2018	Abraham et al.[56]	https://manual.gromacs.org/
VMD Version 1.9.3	Humphrey et al.[57]	https://www.ks.uiuc.edu/Research/vmd/

RESOURCE AVAILABILITY

Lead contact

Further information and requests for resources should be directed to lead contact, Dr. Yuqi Luo (luoyuqi2004@tom.com).

Materials availability

This study did not generate any novel reagents and all materials used in this study are reported either the main text or in the supplemental information.

Data and code availability

- All data reported in this paper will be shared by the lead contact upon request.
- This paper does not report original code.
- Any additional information required to reanalyze the data reported in this paper is available from the lead contact upon request.

METHOD DETAILS

Simulation setup

The subdomain HP35 has only 35 residues and is a fast and independently folding three-helix bundle. Because of its small size and fast folding kinetics, HP35 is a commonly studied protein in MD simulations.[58–60] Therefore, HP35 was chosen as the representative biological system as its folding and unfolding dynamics have been well studied both experimentally and theoretically. The HP35 protein (PDB code: 1YRF [61]) was initially placed above the boridene surface (with the corresponding dimension of 3.587×4.141 nm^2), yielding three simulation systems (as shown in Figure S18). In these three systems, the protein was rotated for 0°, 180°, and 270° to enhance the simulation sampling, finally yielding three simulation systems (i.e., sys-1, sys-2, and sys-3). The closest initial distance between HP35 and boridene was set to over 1.0 nm. Then, these three complexes were immersed in the same box with a dimension of $3.587 \times 4.141 \times 5.000$ nm^3. 0.15 M NaCl and some water molecules were finally added to the boxes, yielding three simulation boxes. More details of simulation boxes are shown in Tables S1 and S3.

Simulation protocol

Molecular dynamics (MD) simulations were carried out using the GROMACS software package (version 2018),[56] and the resulting trajectories were analyzed using VMD software.[57] The CHARMM 36 force field[62] and the TIP3P water model[63] were employed for the protein and water molecules, respectively. The force fields of boridene were derived from a previous study[64] (also see Table S2). The steep algorithm was used for energy minimization. The MD leap-frog integrator[65] was utilized. The temperature and pressure were maintained at 300 K and 1 atm, respectively, using the v-rescale thermostat[66] and the Parrinello-Rahman barostat[67] with semi-isotropic pressure coupling in the z directions (x+y direction was not treated with pressure). Periodic boundary conditions were applied in all directions. Long-range electrostatic interactions were treated using the particle mesh Ewald (PME) method,[68,69] while van der Waals (vdW) interactions were calculated within a cutoff distance of 1.2 nm. Bonds involving hydrogen atoms were constrained to their equilibrium values using the LINCS algorithm,[70] and the SETTLE algorithm[71] was used to constrain the geometry of water molecules. During the simulations, the boridene was fixed. A time step of 2.0 fs was employed, and the coordinates of all atoms were saved every 10 ps. Each system (sys-1, sys-2, and sys-3) was simulated with three parallel trajectories and each trajectory had a 2000-ns duration.